GeoScienceWorld
Lithosphere
Volume 2022, Article ID 4938310, 12 pages
https://doi.org/10.2113/2022/4938310

Lithosphere

Research Article

Stepwise Lithospheric Delamination Leads to Pulsed Cenozoic Uplifts of Central Tien Shan

Haixiang Zhao,[1] **Zhouchuan Huang**,[2] **and Xiaohui Yuan**[3]

[1]*School of Earth Sciences and Engineering, Hohai University, Nanjing, China*
[2]*School of Earth Sciences and Engineering, Nanjing University, Nanjing, China*
[3]*Deutsches GeoForschungsZentrum GFZ, Telegrafenberg, Potsdam, Germany*

Correspondence should be addressed to Haixiang Zhao; zhaohx@hhu.edu.cn and Zhouchuan Huang; huangz@nju.edu.cn

Received 10 September 2022; Revised 1 November 2022; Accepted 23 November 2022; Published 16 December 2022

Academic Editor: Feng Cheng

The Tien Shan provides an ideal site to study mechanism of intracontinental orogeny due to distant effect of Indo-Asian collision. We investigate lithospheric structures, in particular the lithosphere-asthenosphere boundary (LAB), of Central Tien Shan (CTS) using S wave receiver functions. The results show distinct structures across the orogen. Under the southern CTS, the LAB is shallower than that of the Tarim Basin; a 50 km vertical offset implies that part of the lithosphere has been delaminated. Under the middle CTS, two phases of negative velocity gradient are obtained, which may indicate a new LAB and an ongoing delamination underneath. Under the northern CTS and Kazakh Shield northward, the lithosphere is stable although the LAB inclines southward slightly. The two periods of lithospheric delamination under the southern and middle CTS account well for pulsed uplifts of the Tien Shan at ~11-8 Ma and ~5-0 Ma, respectively.

1. Introduction

Intracontinental orogens play important roles in continental evolution of the Earth. On the one hand, the continental orogens mark the termination of the amalgamation between different blocks, through which a large continent or even supercontinent may be formed finally. On the other hand, the intracontinental orogens are usually characterized by weaker rheology than the adjacent blocks and thus are likely to be reactivated first under a new tectonic event. In both cases, the intracontinental orogens experience strong deformation and tectonics. Geological hazards such as large earthquakes occur frequently, which cause heavy damage in general. Therefore, understanding the mechanism of the intracontinental orogens provides insight into the continental cycles and reduces the geological hazards.

The Tien Shan (Figure 1) is a typical continental orogen located in the southern boundary of the Central Asian Orogenic Belt that was formed during the Paleozoic to the Mesozoic (e.g., [1–3]). Its basement includes rigid Precambrian blocks surrounded by various Paleozoic accretion–collision belts [4]. The Tien Shan is divided into the western, central, and eastern Tien Shan through the right lateral Talas-Ferghana Fault and the longitude of ~80°E (the east of the Lake Issyk-Kul) ([4, 5]; Figure 1).

The Central Tien Shan, being situated between Tarim Basin and Pamir (to the south) and Kazakh Shield (to the north), is a natural laboratory to study the rejuvenation mechanism of the Tien Shan orogenic belt. It is further divided into North, Middle, and South Tien Shan (abbreviated as NTS, MTS, and STS, respectively). The Cenozoic orogenesis of the Tien Shan is generally considered distant effect of Indo-Asian collision [4, 6–8] although some studies suggested a potential mantle plume under the Tien Shan (e.g., [9, 10]). Results of apatite fission-track thermochronology, structural modeling, and magnetostratigraphy indicate stepwise uplift of the Tien Shan; the exhumation of the South and North Tien Shan started at 25-15 Ma and 11-10 Ma, respectively [4, 11–15].

GPS measurements show that the Central Tien Shan moves northward relative to the Eurasian Plate ([4, 16]; Figure 1). The rate of the motion decreases linearly from

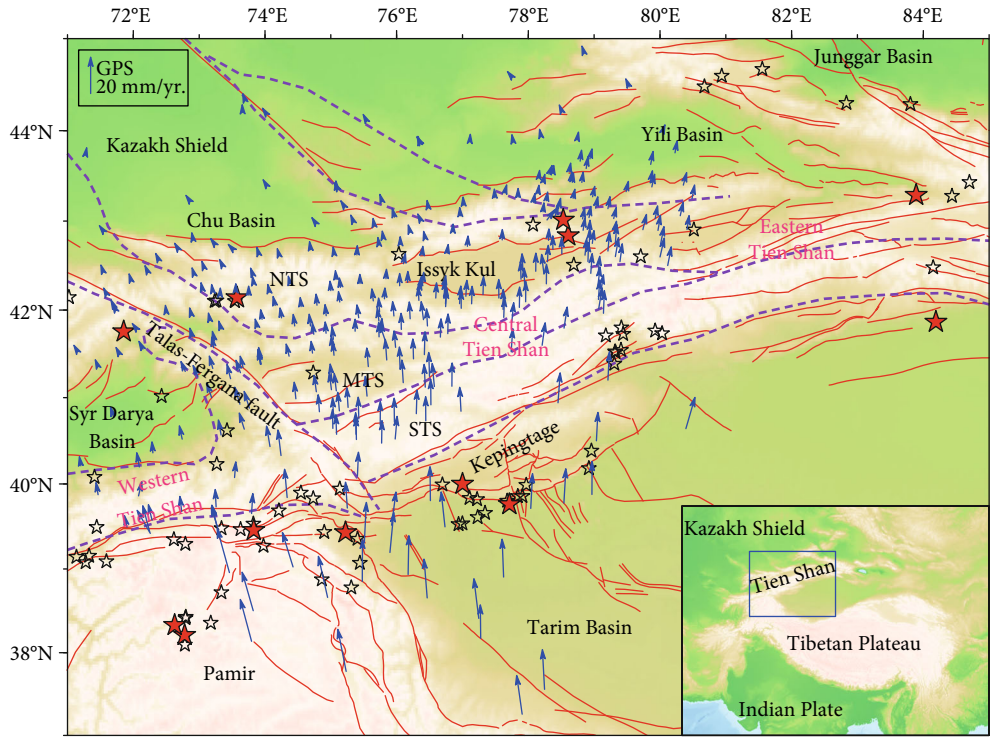

FIGURE 1: Tectonic background. The bottom-right inset shows the location of the study region. Blue arrows denote the GPS observations relative to the stable Eurasian Plate Zubovich et al. [16] with the scale shown at the top-left corner. Dashed purple lines denote the suture zones Brunet et al. [5]. Red lines denote the active faults (https://activefault-datacenter.cn/map). Black and red stars denote the earthquakes of $6.0 \leq M < 7$ and $M \geq 7$, respectively, during 1900 to 2021 (https://earthquake.usgs.gov). Abbreviations: STS: South Tien Shan; MTS: Middle Tien Shan; NTS: North Tien Shan.

~20 mm/yr in the South Tien Shan to <5 mm/yr in the North Tien Shan. The shortening of the South Tien Shan (10 mm/yr) is significantly stronger than that of the North Tien Shan (2-6 mm/yr). Cenozoic crustal shortening is at a scale of ~200 km (e.g., [17]), which contributes only a small portion of the Indo-Asian convergence. However, the shortening estimated from the present GPS measurements is several-fold the levels of the slip rates in the Holocene, implying that the rate of mountain building has been accelerated several times during the past 10 Ma [8, 18].

Deep structures and rheology in the crust and upper mantle are important for understanding the mountain buildings. Seismic results reveal two local depressions of the Moho topography under the South and North Tien Shan where the Moho depths exceed 60 km (e.g., [19–22]). By contrast, the Moho depths are shallower than 50 km under the Tarim Basin, Kazakh Shield, and the Middle Tien Shan. High Vp/Vs ratios (>1.73) under the Central Tien Shan imply the partial melting within the crust, which argues for the magmatic intrusion of the hot upwelling mantle material [19]. Some inclined high velocity anomalies in the upper mantle are proposed to be the subducting Tarim lithosphere under the South Tien Shan and the Kazakh lithosphere under the North Tien Shan [23–28]. Besides, low velocity zones are imaged in the top 150 km under the Central Tien Shan (e.g., [23, 26]). A thicker mantle transition zone was revealed and interpreted to be caused by the detached lithosphere sunk into the transition zone [29–31].

The architecture of the lithosphere plays an essential role in the intracontinental orogens. But images of the lithosphere are unclear in seismic tomography due to the smoothing and smearing effect embedded in the inversion. S wave receiver function (SRF) is a good tool to determine accurate bottom of the lithosphere (i.e., the lithosphere-asthenosphere boundary, LAB hereafter) through S-to-P converted wave (Sp phase) at the LAB. It has been applied in various regions in the work and proven to be a useful method (e.g., [32–34]). A previous study revealed that the LAB depths vary significantly in the Tien Shan, Tarim Basin, and Kazakh Shield [35]. In this study, we determined the LAB of the Central Tien Shan with much improved data set. The improved LAB images provide new insight into the stepwise lithospheric delamination and pulsed uplifts of the Central Tien Shan in the Cenozoic.

2. Data and Method

We collected waveforms from 28 permanent and 99 temporary broadband stations deployed in the Tien Shan from 1997 to 2020 (Figure 2(a)). The 28 permanent stations belong to three networks: KC (2012-2020, 1 station), KN (2010-2020, 10 stations), and KR (2011-2020, 17 stations). The 99 temporary stations belong to three networks: XP (2005-2007, 40 stations), XW (1997-2001, 28 stations), and 8H (2015-2017, 31 stations). A total of 3299 events with epicentral distances of 40-85° and magnitudes ≥ 5.5 were selected (Figures 2(b) and 2(c)), among which 601, 487,

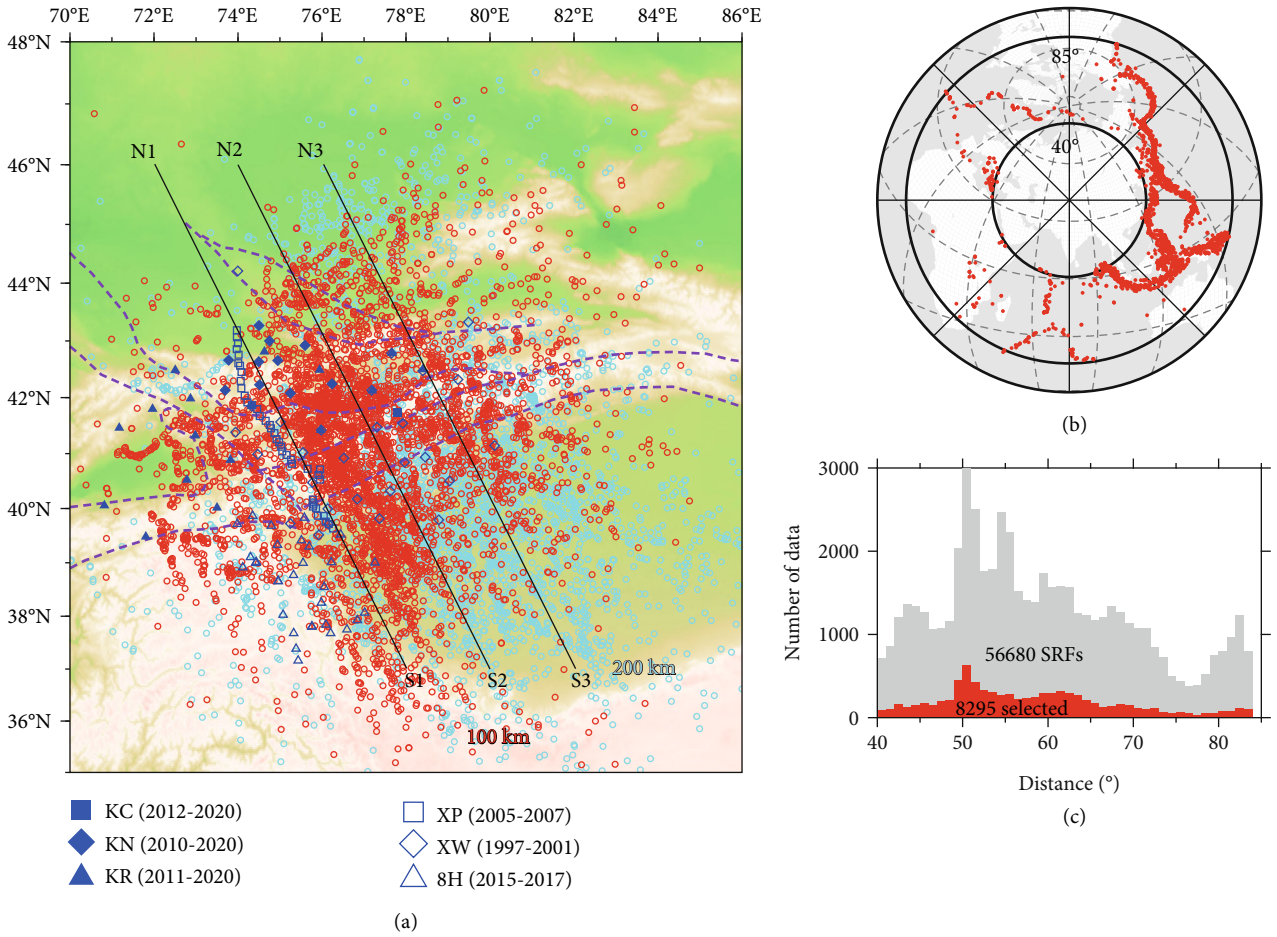

FIGURE 2: Data used in the study. (a) Blue symbols denote the stations of six networks whose labels are shown at the bottom. Red and cyan circles denote the piercing points of the Sp phases at 100 km and 200 km depths, respectively. The black line denotes the profile shown in the following figures. (b) Distribution of the earthquakes used in the study. (c) Epicentral distances of the S wave receiver functions (SRF) calculated in the study. Gray and red columns show the SRFs before and after selection.

280, and 2211 events were recorded by the XW, XP, 8H, and permanent (KC, KN, and KR) stations, respectively. Most of the events are located in western Pacific and Indonesian subduction zones with a back-azimuthal range of 30-160° (Figure 2(b)).

We calculated the SRFs to reveal the LAB beneath the Central Tien Shan by searching for the Sp phase at the LAB [33, 36]. The Sp phases arrive earlier than direct S waves and so are not contaminated by crustal multiples. Because of different velocity gradient at Moho and LAB, the Sp polarities for the Moho and LAB are opposite, i.e., positive for Moho and negative for LAB. To reveal clear and reliable Sp phases, we first removed the noise from seismograms by applying a 4^{th} order zero-phase bandpass Butterworth filter of 1-25 s. Then, we rotated the original Z-E-N components (Figure 3(a)) to the L-Q-T component with the theoretical back-azimuth and incident angles calculated in the IASP91 model [37]. Next, we used a wave-shaping time-domain deconvolution to calculate the SRF, i.e., the L component deconvolved by the corresponding Q component ([38] Figure 3(b)). At last, we used the common-conversion point stacking method to make the SRF profiles [33, 39]. We first projected the SRF in the time domain backward to the points that generate the Sp phases in depth domain; the amplitude at a grid node is obtained by averaging the amplitudes of all the SRFs within a specific distance around the node or along a specific profile. In this study, we further filtered the SRFs with two low-pass filters with the corner frequency of 0.125 Hz (8 s, low frequency) and 0.25 Hz (4 s, high frequency) before constructing the SRF cross-sections, which could reveal the first-order patterns and more details, respectively.

Following Zhao et al. [40], we selected the reliable SRFs automatically based on the signal-to-noise ratios (≥5.0), the shapes and amplitudes on the deconvolved Q and L components. The Q pulse could be well fit by a unit Gaussian function; the correlation efficient is larger than 0.9. The standard deviation and maximum of the amplitudes on the Q and L components before the Q pulse are smaller than 0.1 and 0.25, respectively. The procedure preserved 8295 (i.e., ~15%) high-quality SRFs from 56680 suitable measurements (Figure 2(c)).

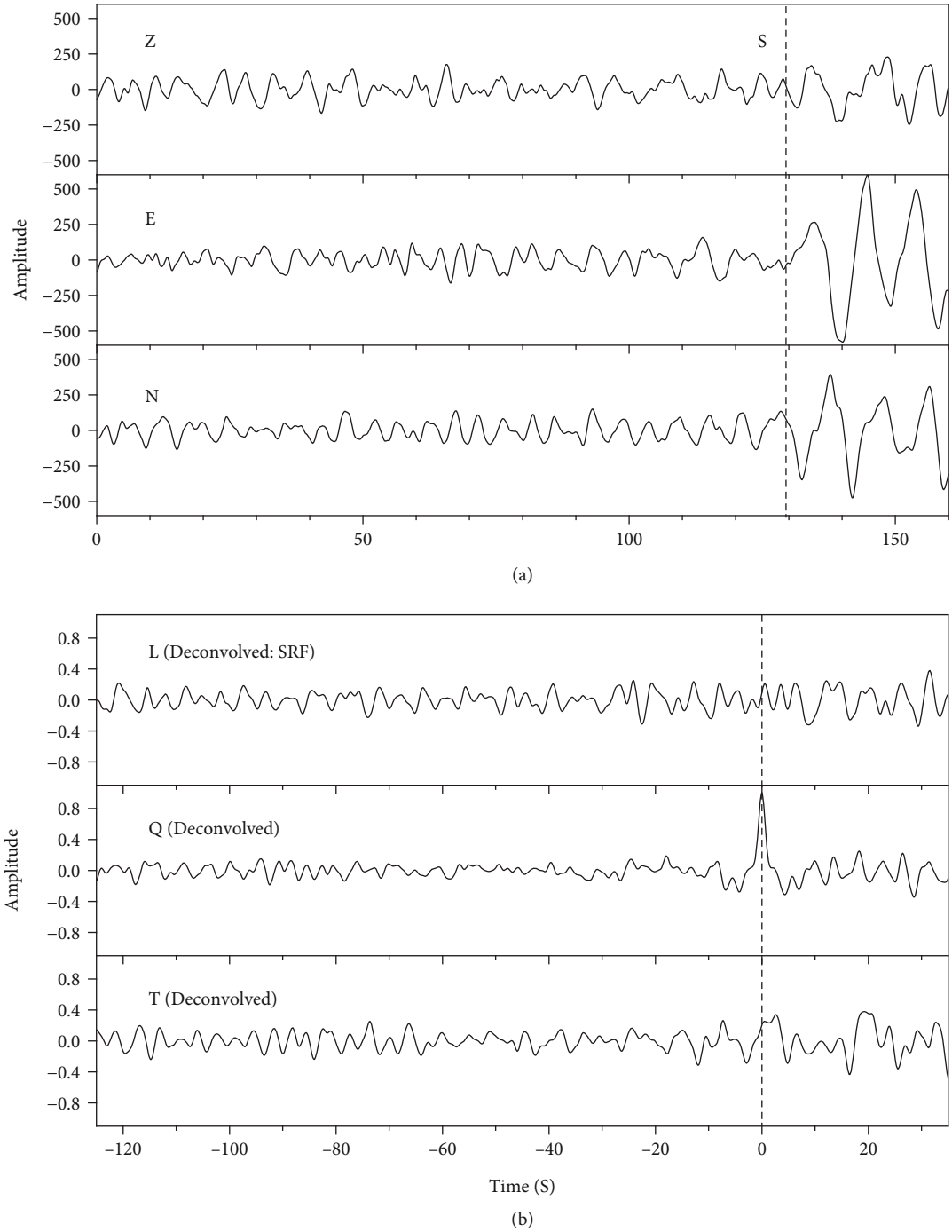

Figure 3: An example of calculating the SRF in Seismic Handler [52]. (a) The original S wave waveforms on the Z-E-N components. (b) The deconvolved L-Q-T components. The deconvolved L component is the obtained SRF.

Notable sidelobes may be caused by the filter and deconvolution in the data processing (e.g., [41]). Because the Q component was processed in the same way as the L component (i.e., the SRF), the sidelobes in the Q component can be used to estimate those in the L component [41]. We corrected the sidelobes in the SRF by referring to the Q component (Figure 4(a)). In the initial SRFs, the negative signal below the Moho is notable in the whole sections (Figures 4(b) and 4(d)). However, most of these negative signals are removed after the SRFs were corrected with the Q component except for those under the South Tien Shan (Figures 4(c) and 4(e)).

To estimate the uncertainty of the obtained SRFs, we used a bootstrapping method to estimate the uncertainties of the SRF images. We selected 60% of the data set randomly and calculated the corresponding SRFs 1000 times. The average and standard deviation of the 1000 SRFs were taken as the final SRF and its uncertainty, respectively. A LAB

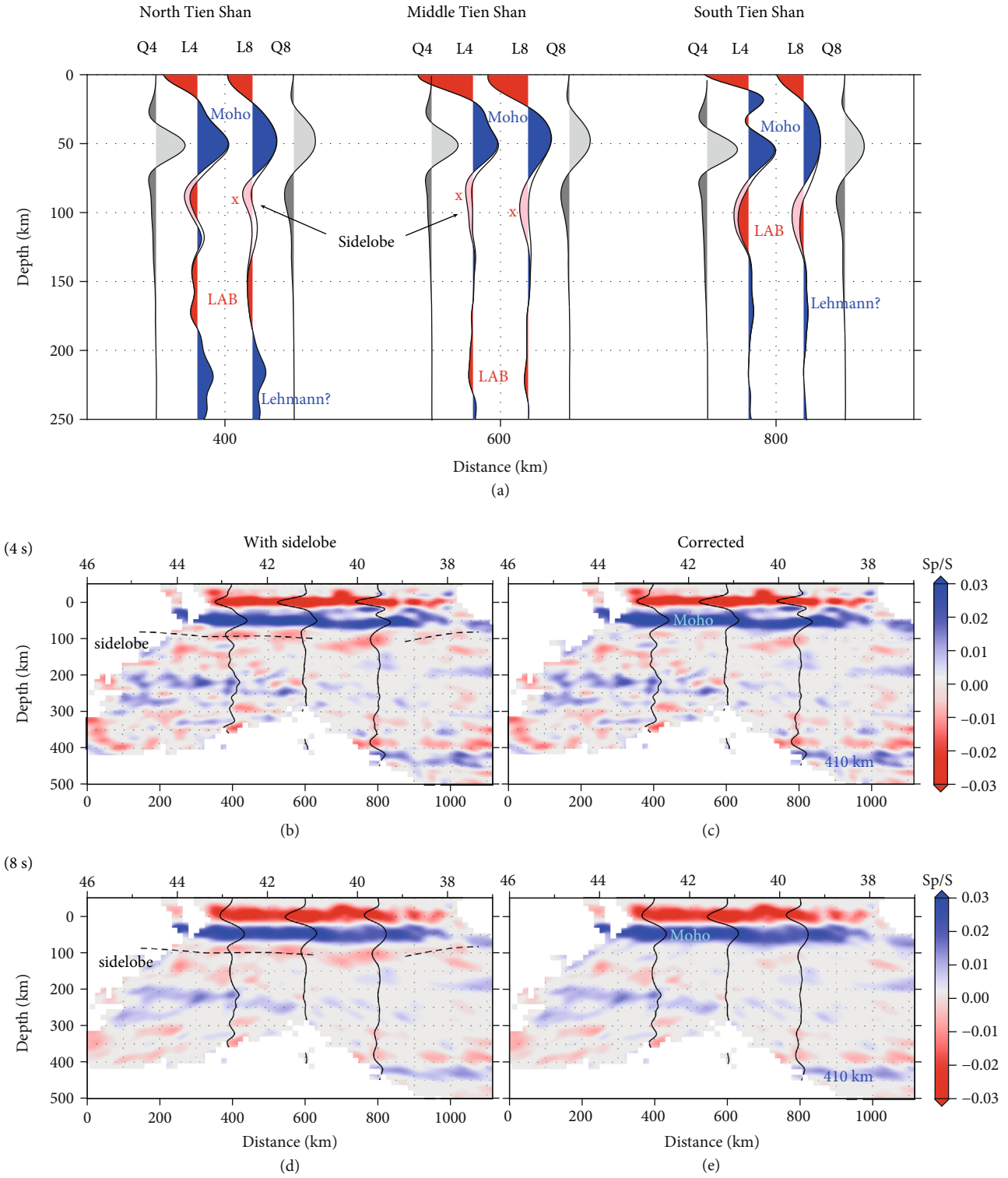

Figure 4: Analysis of the sidelobes. (a) Red and pink colors show the negative phases in SRFs filtered by a low-pass filter above 4 s (L4) and 8 s (L8) while blue colors show the positive phases. Light gray pulses denote the corresponding Q components (Q4 and Q8), the maximum amplitudes of which are normalized and aligned to the Moho phases in the SRFs; the dark gray colors are caused by the sidelobes. The red crosses mark the negative SRF phases (pink shaded) caused by the sidelobes in data processing, which are removed in the corrected SRFs. LAB: lithosphere-asthenosphere boundary. (b, c) The initial and corrected SRF images filtered above 4 s along the NW-SE direction shown in Figure 2(a). Blue and red colors show the positive and negative SRF phases as the scale shown at the bottom-right. The horizontal dashed lines mark the negative phases due to the sidelobes. The Moho and 410 discontinuities are indicated. (d, e) The same as (b, c) but for the SRFs filtered above 8 s.

signal is reliable only when its upper limit is negative after the uncertainty is corrected from the mean value.

3. Results

Figure 5 shows the stacked images along the NW-SE direction (Figure 2(a)); all SRFs are projected to the profile. As two most important discontinuities in the upper mantle, the Moho and 410 km discontinuities are clear (Figures 4 and 5). The Moho topography correlates well with that determined by the P wave receiver functions (PRF; [20, 22]) which has generally higher resolution thanks to the higher frequency. The clear Moho and 410 km discontinuities imply that the obtained Sp signals are reliable in the upper mantle, in particular those signals between the Moho and 410 km discontinuities. At the same time, the depths of the Moho and 410 km discontinuities provide proper estimate of the uncertainties of the LAB depths caused by the velocity anomalies in the upper mantle. Compared with the PRF results [20, 22, 31], the uncertainties of the Moho and 410 km discontinuities' depths are ~5 km and ~10 km, respectively (Figure 5). Therefore, the uncertainties of the LAB depths in between are smaller than 5-10 km in general.

In the lithospheric domain (i.e., above 200 km), the SRF features vary laterally under different regions. The polarity of the LAB signals is negative because the velocity gradient is opposite to those at the Moho and 410 km discontinuities. Under the Tarim Basin, northward-dipped negative phases are found at ~120-170 km depth (T). Under the South Tien Shan, northward-dipped negative phases are imaged at 100-130 km depths (D1) right below the Moho. Under the Middle Tien Shan, two negative phases are revealed around 100 km (D2) and 200 km depth (Dx), respectively. The signal Dx dips northward slightly while the dipping feature of D2 is unclear. Under the North Tien Shan and Kazakh Shield, negative phases are imaged between 120 and 200 km depths. The negative phases dip southward in the low-frequency image (Figure 5(c)). However, they show apparent double phases in the high-frequency image, one at ~120-140 km depth (K1) while another at ~160-200 km depth (K2) (Figure 5(b)). A small negative phase (D3) is also imaged at 90 km under the North Tien Shan, but its lateral extent is limited.

We also investigated the variation of the SRFs along the strike (i.e., WSW-ENE) of the Central Tien Shan (Figure 6). In all these profiles, the negative phases under the South Tien Shan (D1) are robust, in both high-frequency (4 s) and low-frequency images (8 s), confirming that they are generated by the actual structures rather than sidelobes. The negative phases under the Tarim Basin (T) and Kazakh Shield (K1 and K2) are also robust, being consistent with the regional features (Figure 5). The negative phases under the Middle Tien Shan (D2 and Dx) are more prominent in the high-frequency images than in the low-frequency images, but they are visible in all profiles. The shallow negative phases under the North Tien Shan (D3) are clearer in the high-frequency images, but they are almost absent in the low-frequency images. In a short summary, the along-strike variations of the SRFs in the Central Tien Shan are insignificant; the structures change across the orogen in general in the NW-SE direction.

The negative phases described above generally represent the LAB in Central Tien Shan. The LAB depths are consistent with those determined by Kumar et al. [35] under the South Tien Shan and the Tarim Basin (Figures 5(b) and 5(c)). By contrast, under the North and Middle Tien Shan, the LAB of Kumar et al. [35] is located at ~100 km, which is consistent with the weak negative signals in the high-frequency image (Figure 5(b)).

Another notable feature is the positive phase (L) under the LAB, which extends between 200 km and 300 km depths under the Kazakh Shield and Tien Shan and around 200 km depth under the Tarim Basin. They are parallel to the LABs (K2 and T) above, showing opposite trends toward the Tien Shan. The L phases may represent the Lehmann discontinuity that is the bottom of the asthenosphere [42].

4. Discussions

The Cenozoic evolution of the Tien Shan is controlled by the distant effect of the Indo-Asian collision [4, 6–8, 43]. The Central Tien Shan is characterized by strong lateral variations in north-south direction. The southern part (i.e., South Tien Shan) has high topography, strain rate, and seismicity. In contrast, in the northern part (Middle and North Tien Shan), the topography includes various ridges and depressions; both the strain rate and seismicity are weaker than those in the South Tien Shan. In the time domain, the uplift started earlier in the South Tien Shan than in the North Tien Shan. The dominant features in the SRF images also change in north-south direction in general while the east-west variation is weak.

4.1. South Tien Shan. Under the South Tien Shan, the LAB is located at ~100-130 km depths (D1); it dips northward (Figure 5). Seismic tomography revealed a clear northward-dipped high-velocity body in the upper mantle that was generally interpreted as the Tarim lithosphere under the South Tien Shan [23–28, 44]. Detailed crustal structures favor northern intrusion or underthrust of the Tarim lithosphere rather than subduction [20, 45]. Our SRF images are consistent with a possible northward intrusion. This model may account for the initial uplift of the South Tien Shan in ~25-15 Ma [12, 14, 15].

However, the LABs are not continuous under the South Tian Shan and Tarim Basin; there is a ~50 km offset in depth (Figure 5). We propose that the lower part of the lithosphere under the South Tien Shan has been delaminated. P wave receiver functions revealed uplifted 410 km discontinuity and thickened mantle transition zone under the South Tien Shan [29–31], suggesting that the delaminated lithosphere has sunk into the transition zone. The delamination and subsequent mantle upwelling may cause another uplift of the South Tien Shan in ~10-8 Ma [12, 14, 15]. The upwelling explains the partial melting in the crust of the South Tien Shan that was expressed as low velocities and high Vp/Vs ratios [19, 22, 24, 46].

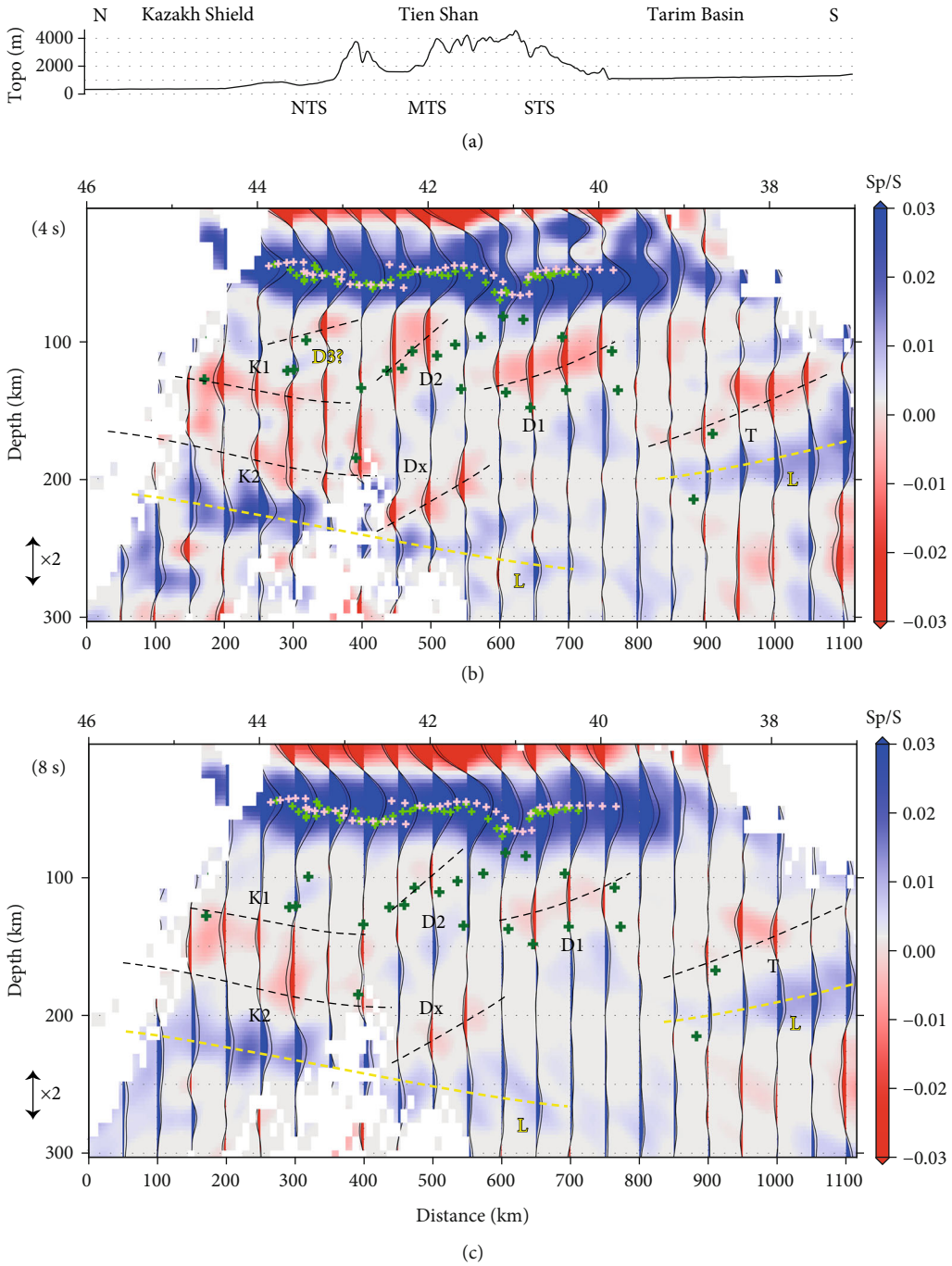

Figure 5: The SRF images along the NW-SE direction. (a) The topography along the profile N2-S2 shown in Figure 2(a). NTS, MTS, and STS denote North, Middle, and South Tien Shan, respectively. (b, c) The SRF images filtered by a low-pass filter above 4 s and 8 s, respectively. Blue and red colors show the positive and negative SRF phases as the scale shown at the right. The average SRFs are shown as wiggles every 50 km along the profile; the filled colors show the lower limit of the SRF after the standard deviation is considered. The results at the grid nodes with number of SRFs smaller than 5 are masked. Negative LAB phases below different tectonic regions are marked by dashed lines and labeled. Light green and red crosses denote the Moho determined by Zhang et al. [22] and Li et al. [20], respectively; dark green crosses show the LAB determined by Kumar et al. [35]. Note that the latitudes of the measurements may deviate from the original values because they are projected to the profile to the northwest.

4.2. Middle Tien Shan. Under the Middle Tien Shan, the LAB structures are complex. Two plausible negative Sp phases are visible in the upper mantle, one weak phase at ~100 km depth (D2) while another at ~200 km depth (Dx) (Figure 5). Dx is deeper than the LAB under the Kazakh Shield and Tarim Basin, so it is not likely the LAB under the orogen. Here, we interpret that Dx represents the newly delaminated lithosphere while D2 is the new LAB after the lithospheric delamination.

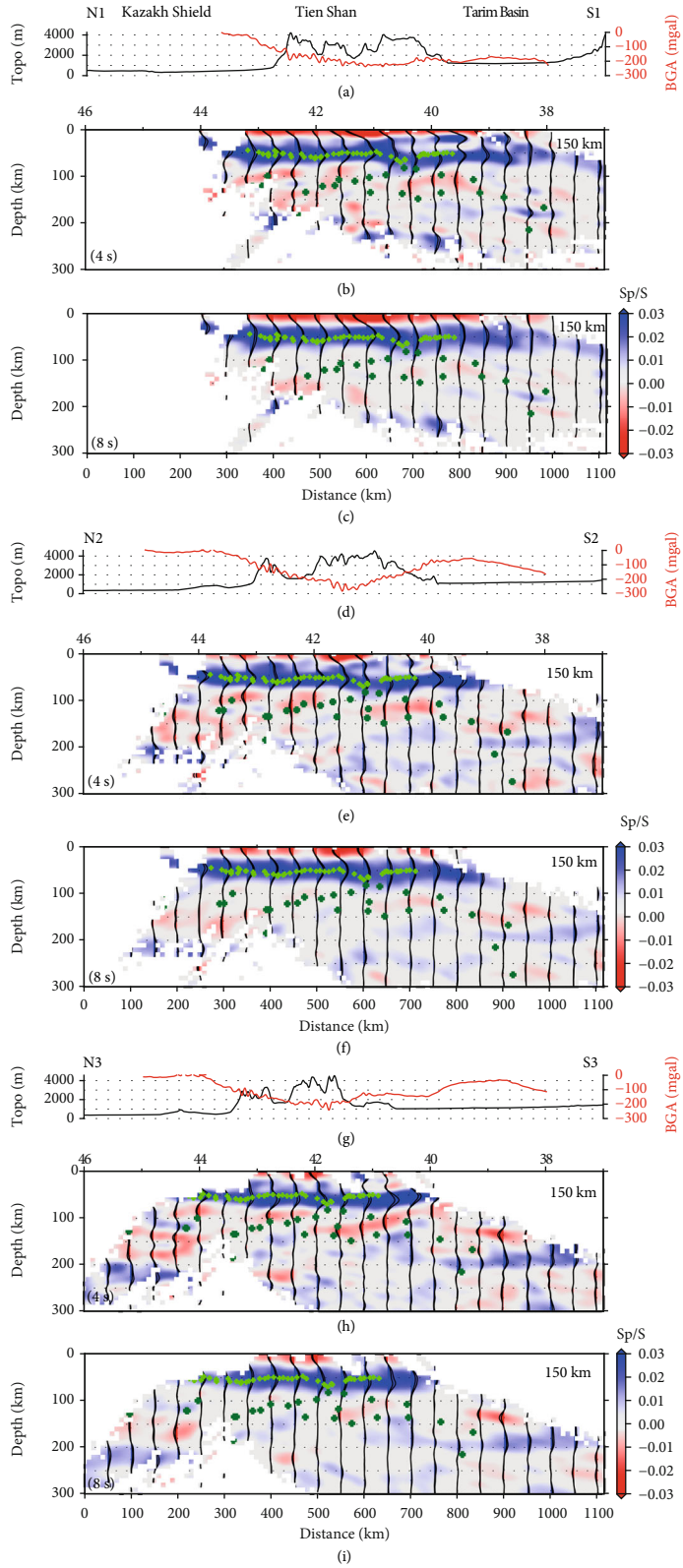

FIGURE 6: The SRF images along three profiles shown in Figure 2(a). Only the SRFs whose piercing points are located within 150 km from the profiles are included and averaged. Red lines at the top show the Bouguer gravity anomalies (BGA) along the profiles Bonvalot et al. [54]. For the other labeling, see Figure 5.

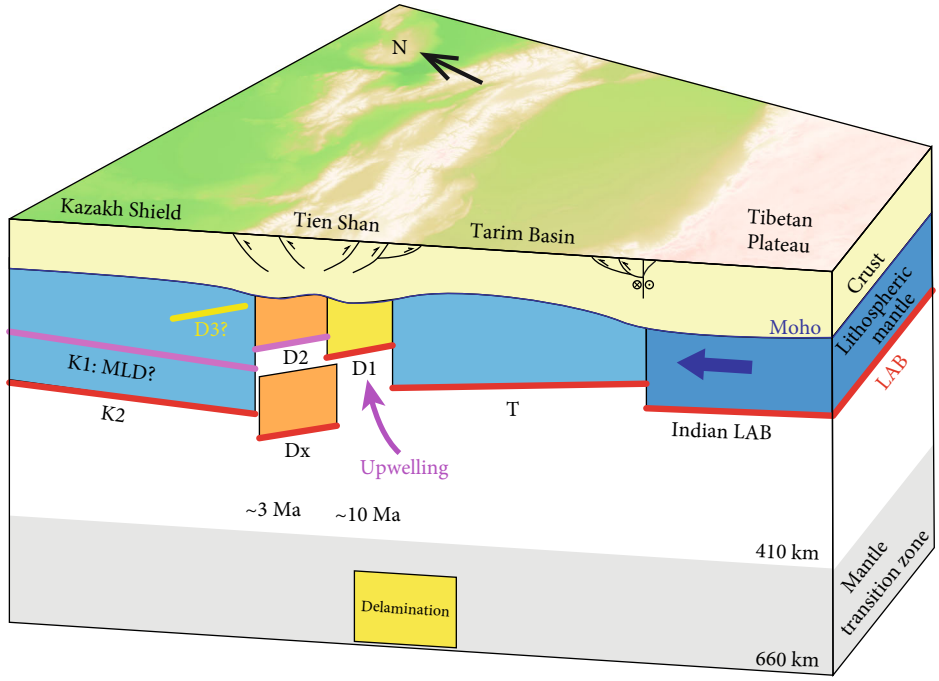

FIGURE 7: A conceptual model of the stepwise lithospheric delamination under the Tien Shan in the Cenozoic. D1 and D2 mark two possible delaminations occurring at ~10 Ma and ~3 Ma, respectively.

Because the delamination is in an early stage, the response at surface is indistinctive as widespread mantle upwelling has not developed. However, two observations still argue that the delamination occurs under the Middle Tien Shan. First, the Bouguer gravity anomalies show strong negative values (Figure 6) that cannot be matched by regional compensation of a continuous elastic plate under the Tien Shan; mantle downwelling is required to explain the gravity anomalies [47, 48]. Thus, the initial-stage delamination without significant mantle upwelling is a good candidate to the measured gravity anomalies. Second, the delamination promoted the second exhumation of the North Tien Shan. Taking the speed of delamination of ~3-5 cm/yr [49], a 50-100 km distance of delamination (as compared with the adjacent LAB) implies that the delamination under the Middle Tien Shan started at ~3-1 Ma. The estimated time is consistent with the latest rapid exhumation of the North Tien Shan at 3-0 Ma and the South Tien Shan at ~3-2 Ma [4, 11, 12]. Therefore, we suggest that the lithospheric delamination under the Middle Tien Shan reduced the strength of the lithosphere so that the crustal deformation and uplift in the adjacent South and North Tien Shan were accelerated.

4.3. North Tien Shan and Kazakh Shield. Under the North Tien Shan and Kazakh Shield, two negative Sp phases are located at ~120-140 km (K1) and ~160-200 km (K2) depths, respectively; they slightly dip southward (Figure 5). The horizontally consistent structures in these two regions indicate that the lithospheric mantle of the North Tien Shan has not been deformed in general as below the South and Middle Tien Shan. Therefore, the uplift of the North Tien Shan was caused solely by crustal deformation (e.g., [20, 45]). The slightly dipped plane may be formed by the crustal load as the North Tien Shan (e.g., [8, 11]. In fact, the two pulses of deformation in the North Tien Shan, i.e., 11-10 Ma and 3-0 Ma [11], are correlated with the lithospheric delamination occurring in the South and Middle Tien Shan as proposed above, being consistent with the model of crustal deformation in response of the lithospheric delamination under convergence (e.g., [43]).

Yet another two questions need to be addressed: what do the two negative phases (K1, K2) represent? Will the lithospheric delamination propagate northward further? They could be well answered if the upper negative phase (K1) represents the middle lithospheric discontinuity (MLD). The MLD is usually observed within the lithosphere under continents, especially the craton (e.g., [50, 51]). It may be a thin layer of partial melting that separate different layers of compositions or deformations in the lithosphere [50]. The MLD signal in our images is located at ~120-140 km, being deeper than the global averages [50, 51]. But if the upper mantle contains volumes of hydrous minerals, notable negative velocity gradients can be generated below 120 km depth [51]. Therefore, we regard the negative Sp phases at ~120-140 km as the MLD under the North Tien Shan and Kazakh Shield. The MLD is a weak layer, so the lower part of the lithosphere would be detached along the MLD [50]. In particular, as the delaminated lithosphere under the Middle Tien Shan sinks further, the asthenospheric material will rise and erode the adjacent lithosphere. Therefore, the delamination is expected to propagate northward under the North Tien Shan and Kazakh Shield in the future. Phase D3 provides another way for the potential delamination. If it is the same structure as phases D1 and D2 under the South and Middle Tien Shan, the whole lithosphere may be

delaminated instead of the lower part of the lithosphere through the MLD (K1). However, the data coverage is poorer than those under the South Tien Shan and Tarim Basin (Figures 2(a) and 4–6); thus, improved observations are necessary to better understand the structures under the North Tien Shan and Kazakh Shield.

5. Conclusions

We imaged the lithospheric structures beneath the Central Tien Shan using S wave receiver functions (SRF). The SRF images show distinct features across the orogen in the north-south direction. A conceptual model is shown in Figure 7. The main findings are summarized as follows:

(1) Delamination has occurred beneath the South and Middle Tien Shan. The delaminated lithosphere has sunk into the mantle transition zone under the South Tien Shan while the process is in the initial stage under the Middle Tien Shan. The lithosphere under the North Tien Shan is still stable, but the delamination may propagate northward as a plausible MLD is imaged in the lithosphere underneath

(2) The uplift of the Central Tien Shan is closely related to the lithospheric delamination. While the initial uplift (~25-15 Ma) is caused by the lateral shortening due to the distant effect of the Indo-Asian collision, the latter two pulsed uplifts (~10 Ma and~3 Ma) coincide with delamination under the South and Middle Tien Shan. The delamination reduced the lithospheric strength significantly, so the uplift of the Tien Shan was accelerated following the delamination

Data Availability

The data were downloaded freely from the Incorporated Research Institutions for Seismology (IRIS) Data Center (10.7914/SN/KC, 10.7914/SN/KN, 10.7914/SN/KR, 10.7914/SN/XP_2005, and 10.7914/SN/XW_1997) and the GEOFON data centre of the GFZ German Research Centre for Geosciences (doi:10.14470/3U7560589977).

Conflicts of Interest

The authors declare that there is no conflict of interest.

Acknowledgments

This work is supported by the National Natural Science Foundations of China (41203011 and 42174056). ZH is also supported by the Deng-Feng Scholar Program of Nanjing University. The S wave receiver functions were calculated using Seismic Handler [52]. The numerical calculations in this paper have been done on the computing facilities in the High Performance Computing Center of Nanjing University. The figures were made using GMT [53].

References

[1] A. M. C. Şengör, B. A. Natal'in, and V. S. Burtman, "Evolution of the Altaid tectonic collage and Palaeozoic crustal growth in Eurasia," *Nature*, vol. 364, no. 6435, pp. 299–307, 1993.

[2] B. F. Windley, M. B. Allen, C. Zhang, Z.-Y. Zhao, and G.-R. Wang, "Paleozoic accretion and Cenozoic redeformation of the Chinese Tien Shan range, central Asia," *Geology*, vol. 18, no. 2, pp. 128–131, 1990.

[3] W. Xiao, B. F. Windley, S. Sun et al., "A tale of amalgamation of three Permo-Triassic collage systems in Central Asia: oroclines, sutures, and terminal accretion," *Annual Review of Earth and Planetary Sciences*, vol. 43, no. 1, pp. 477–507, 2015.

[4] M. M. Buslov, J. De Grave, E. A. V. Bataleva, and V. Y. Batalev, "Cenozoic tectonic and geodynamic evolution of the Kyrgyz Tien Shan mountains: a review of geological, thermochronological and geophysical data," *Journal of Asian Earth Sciences*, vol. 29, no. 2–3, pp. 205–214, 2007.

[5] M.-F. Brunet, E. R. Sobel, and T. McCann, "Geological evolution of Central Asian basins and the western Tien Shan range," *Geological Society, London, Special Publications*, vol. 427, no. 1, pp. 1–17, 2017.

[6] L. M. Flesch, A. J. Haines, and W. E. Holt, "Dynamics of the India-Eurasia collision zone," *Journal of Geophysical Research: Solid Earth*, vol. 106, no. B8, pp. 16435–16460, 2001.

[7] P. Tapponnier, G. Peltzer, A. Y. L. Dain, R. Armijo, and P. Cobbold, "Propagating extrusion tectonics in Asia: new insights from simple experiments with plasticine," *Geology*, vol. 10, no. 12, pp. 611–616, 1982.

[8] V. S. Burtman, "Geodynamics of Tibet, Tarim, and the Tien Shan in the Late Cenozoic," *Geotectonics*, vol. 46, no. 3, pp. 185–211, 2012.

[9] L. I. Makeyeva, L. P. Vinnik, and S. W. Roecker, "Shear-wave splitting and small-scale convertion in the continental upper mantle," *Nature*, vol. 358, pp. 144–147, 1992.

[10] E. R. Sobel and N. Arnaud, "Cretaceous-Paleogene basaltic rocks of the Tuyon basin, NW China and the Kyrgyz Tian Shan: the trace of a small plume," *Lithos*, vol. 50, no. 1–3, pp. 191–215, 2000.

[11] M. E. Bullen, D. W. Burbank, and J. I. Garver, "Building the northern Tien Shan: integrated thermal, structural, and topographic constraints," *The Journal of Geology*, vol. 111, no. 2, pp. 149–165, 2003.

[12] S. Glorie, J. De Grave, M. M. Buslov et al., "Tectonic history of the Kyrgyz South Tien Shan (Atbashi-Inylchek) suture zone: the role of inherited structures during deformation-propagation," *Tectonics*, vol. 30, no. 6, 2011.

[13] E. A. Macaulay, E. R. Sobel, A. Mikolaichuk, B. Kohn, and F. M. Stuart, "Cenozoic deformation and exhumation history of the central Kyrgyz Tien Shan," *Tectonics*, vol. 33, no. 2, pp. 135–165, 2014.

[14] E. Sobel, J. Chen, and R. Heermance, "Late Oligocene-Early Miocene initiation of shortening in the Southwestern Chinese Tian Shan: Implications for Neogene shortening rate variations," *Earth and Planetary Science Letters*, vol. 247, no. 1–2, pp. 70–81, 2006.

[15] E. R. Sobel and T. A. Dumitru, "Thrusting and exhumation around the margins of the western Tarim basin during the India-Asia collision," *Journal of Geophysical Research: Solid Earth*, vol. 102, no. B3, pp. 5043–5063, 1997.

[16] A. V. Zubovich, X. Wang, Y. G. Scherba et al., "GPS velocity field for the Tien Shan and surrounding regions," *Tectonics*, vol. 29, no. 6, 2010.

[17] J. P. Avouac, P. Tapponnier, M. Bai, H. You, and G. Wang, "Active thrusting and folding along the northern Tien Shan and Late Cenozoic rotation of the Tarim relative to Dzungaria and Kazakhstan," *Journal of Geophysical Research: Solid Earth*, vol. 98, no. B4, pp. 6755–6804, 1993.

[18] K. Y. Abdrakhmatov, S. A. Aldazhanov, B. H. Hager et al., "Relatively recent construction of the Tien Shan inferred from GPS measurements of present-day crustal deformation rates," *Nature*, vol. 384, no. 6608, pp. 450–453, 1996.

[19] Q. Cui, Y. Zhou, J. Li, X. Song, Y. Gao, and R. Cui, "Crustal thickness (H) and Vp/Vs ratio (κ) images beneath the central Tien Shan revealed by the H - κ - c method," *Tectonophysics*, vol. 822, article 229157, 2022.

[20] W. Li, Y. Chen, X. Yuan, W. Xiao, and B. F. Windley, "Intracontinental deformation of the Tianshan Orogen in response to India- Asia collision," *Nature Communications*, vol. 13, no. 1, p. 3738, 2022.

[21] L. P. Vinnik, C. Reigber, I. M. Aleshin et al., "Receiver function tomography of the central Tien Shan," *Earth and Planetary Science Letters*, vol. 225, no. 1–2, pp. 131–146, 2004.

[22] B. Zhang, X. Bao, and Y. Xu, "Distinct orogenic processes in the south- and north-central Tien Shan from receiver functions," *Geophysical Research Letters*, vol. 47, no. 6, article e2019GL086941, 2020.

[23] J. Lei and D. Zhao, "Teleseismic P-wave tomography and the upper mantle structure of the central Tien Shan orogenic belt," *Physics of the Earth and Planetary Interiors*, vol. 162, no. 3–4, pp. 165–185, 2007.

[24] L. Zhiwei, S. Roecker, L. Zhihai et al., "Tomographic image of the crust and upper mantle beneath the western Tien Shan from the MANAS broadband deployment: possible evidence for lithospheric delamination," *Tectonophysics*, vol. 477, no. 1–2, pp. 49–57, 2009.

[25] Z. Lü, J. Lei, L. Zhao et al., "Crustal deformation of intermontane basins beneath central Tien Shan revealed by full-wave ambient noise tomography," *Tectonophysics*, vol. 821, article 229143, 2021.

[26] S. W. Roecker, T. M. Sabitova, L. P. Vinnik et al., "Three-dimensional elastic wave velocity structure of the western and central Tien Shan," *Journal of Geophysical Research*, vol. 98, no. B9, p. 15779, 1993.

[27] I. V. Sychev, I. Koulakov, N. A. Sycheva et al., "Collisional processes in the crust of the northern Tien Shan inferred from velocity and attenuation tomography studies," *Journal of Geophysical Research: Solid Earth*, vol. 123, no. 2, pp. 1752–1769, 2018.

[28] J. Zhao, G. Liu, Z. Lu, X. Zhang, and G. Zhao, "Lithospheric structure and dynamic processes of the Tianshan orogenic belt and the Junggar basin," *Tectonophysics*, vol. 376, no. 3–4, pp. 199–239, 2003.

[29] Y. H. Chen, S. W. Roecker, and G. L. Kosarev, "Elevation of the 410 km discontinuity beneath the central Tien Shan: evidence for a detached lithospheric root," *Geophysical Research Letters*, vol. 24, no. 12, pp. 1531–1534, 1997.

[30] X. Tian, D. Zhao, H. Zhang, Y. Tian, and Z. Zhang, "Mantle transition zone topography and structure beneath the central Tien Shan orogenic belt," *Journal of Geophysical Research: Solid Earth*, vol. 115, no. B10, p. B10308, 2010.

[31] Y. Yu, D. Zhao, and J. Lei, "Mantle transition zone discontinuities beneath the Tien Shan," *Geophysical Journal International*, vol. 211, no. 1, pp. 80–92, 2017.

[32] V. Farra and L. Vinnik, "Upper mantle stratification by P and S receiver functions," *Geophysical Journal International*, vol. 141, no. 3, pp. 699–712, 2000.

[33] R. Kind, X. Yuan, and P. Kumar, "Seismic receiver functions and the lithosphere-asthenosphere boundary," *Tectonophysics*, vol. 536-537, pp. 25–43, 2012.

[34] C. Rychert and P. Shearer, "A global view of the lithosphere-asthenosphere boundary," *Science*, vol. 324, no. 5926, pp. 495–498, 2009.

[35] P. Kumar, X. Yuan, R. Kind, and G. Kosarev, "The lithosphere-asthenosphere boundary in the Tien Shan-Karakoram region from S receiver functions: Evidence for continental subduction," *Geophysical Research Letters*, vol. 32, no. 7, p. L07305, 2005.

[36] X. Yuan, R. Kind, X. Li, and R. Wang, "The S receiver functions: synthetics and data example," *Geophysical Journal International*, vol. 165, no. 2, pp. 555–564, 2006.

[37] B. L. N. Kennett and E. R. Engdahl, "Traveltimes for global earthquake location and phase identification," *Geophysical Journal International*, vol. 105, no. 2, pp. 429–465, 1991.

[38] R. W. Clayton and R. A. Wiggins, "Source shape estimation and deconvolution of teleseismic body waves," *Geophysical Journal International*, vol. 47, no. 1, pp. 151–177, 1976.

[39] G. Kosarev, R. Kind, S. V. Sobolev, X. Yuan, W. Hanka, and S. Oreshin, "Seismic evidence for a detached Indian lithospheric mantle beneath Tibet," *Science*, vol. 283, no. 5406, pp. 1306–1309, 1999.

[40] H. Zhao, P. Wang, and Z. Huang, "Lithospheric structures beneath the western Mongolian Plateau: insight from S wave receiver function," *Journal of Asian Earth Sciences*, vol. 212, article 104733, 2021.

[41] R. Kind, W. D. Mooney, and X. Yuan, "New insights into the structural elements of the upper mantle beneath the contiguous United States from S-to-P converted seismic waves," *Geophysical Journal International*, vol. 222, no. 1, pp. 646–659, 2020.

[42] R. Kind and X. Li, "Deep earth structure - transition zone and mantle discontinuities," *Geophysics*, vol. 1, pp. 655–682, 2015.

[43] P. Huangfu, Z. H. Li, K. J. Zhang, W. Fan, J. Zhao, and Y. Shi, "India-Tarim lithospheric mantle collision beneath western Tibet controls the Cenozoic building of Tian Shan," *Geophysical Research Letters*, vol. 48, no. 14, article e2021GL094561, 2021.

[44] V. I. Makarov, D. V. Alekseev, V. Y. Batalev et al., "Underthrusting of Tarim beneath the Tien Shan and deep structure of their junction zone: main results of seismic experiment along MANAS profile Kashgar-Song-Köl," *Geotectonics*, vol. 44, no. 2, pp. 102–126, 2010.

[45] B. Zhang, X. Bao, and Y. Xu, "Seismic anisotropy in the central Tien Shan unveils rheology-controlled deformation during intracontinental orogenesis," *Geology*, vol. 50, no. 7, pp. 812–816, 2022.

[46] A. Gilligan, S. W. Roecker, K. F. Priestley, and C. Nunn, "Shear velocity model for the Kyrgyz Tien Shan from joint inversion of receiver function and surface wave data," *Geophysical Journal International*, vol. 199, no. 1, pp. 480–498, 2014.

[47] E. V. Burov, M. G. Kogan, H. Lyon-Caen, and P. Molnar, "Gravity anomalies, the deep structure, and dynamic processes

beneath the Tien Shan," *Earth and Planetary Science Letters*, vol. 96, no. 3–4, pp. 367–383, 1990.

[48] X. Jiang, "Dynamic support of the Tien Shan lithosphere based on flexural and rheological modeling," *Journal of Asian Earth Sciences*, vol. 93, pp. 37–48, 2014.

[49] E. Hafkenscheid, M. J. R. Wortel, and W. Spakman, "Subduction history of the Tethyan region derived from seismic tomography and tectonic reconstructions," *Journal of Geophysical Research: Solid Earth*, vol. 111, no. B8, p. B08401, 2006.

[50] L. Chen, "Layering of subcontinental lithospheric mantle," *Science Bulletin*, vol. 62, no. 14, pp. 1030–1034, 2017.

[51] K. Selway, H. Ford, and P. B. Kelemen, "The seismic mid-lithosphere discontinuity," *Earth and Planetary Science Letters*, vol. 414, pp. 45–57, 2015.

[52] K. Stammler, "Seismichandler–programmable multichannel data handler for interactive and automatic processing of seismological analyses," *Computers Geosciences*, vol. 19, no. 2, pp. 135–140, 1993.

[53] P. Wessel, J. F. Luis, L. Uieda et al., "The generic mapping tools version 6," *Geochemistry, Geophysics, Geosystems*, vol. 20, no. 11, pp. 5556–5564, 2019.

[54] S. Bonvalot, G. Balmino, A. Briais et al., *World Gravity Map*, BGI-CGMW-CNES-IRD, Paris, 2012.